remote sensing

Article

Distinguishing Dominant Drivers on LST Dynamics in the Qinling-Daba Mountains in Central China from 2000 to 2020

Mengzhu Xi [1,2,3], Wen Zhang [1,2,3], Wanlong Li [1,2,3], Haodong Liu [1,2,3] and Hui Zheng [1,2,3,*]

[1] Key Laboratory of Geospatial Technology for Middle and Lower Yellow River Regions, Ministry of Education, College of Environment and Planning, Henan University, Kaifeng 475004, China
[2] Henan Key Laboratory of Earth System Observation and Modeling, Henan University, Kaifeng 475004, China
[3] Henan Key Laboratory of Integrated Air Pollution Control and Ecological Security, Kaifeng 475004, China
[*] Correspondence: zhenghui@vip.henu.edu.cn

Abstract: Land surface temperature (LST) is an important driving factor in the land-atmosphere energy cycle. To examine the spatiotemporal patterns of LST changes and the internal mechanisms driven by multiple factors, we used a trend analysis method on TRIMS LST data from 2000 to 2020 in the Qingling-Daba Mountains. The optimal parameter geographic detector (OPGD) model was used to detect the influence of twelve factors, including elevation, precipitation, albedo, relative humidity (RH) and normalized difference vegetation index (NDVI), on the spatial distribution of LST, as well as to explore the dominant factors affecting LST differentiation in the study area. The results showed that: (1) From 2000 to 2020, the average annual LST of the Qinling-Daba Mountains was 18.17 °C. The warming trend was obvious (0.034 °C/a), and the warming effect at nighttime (0.066 °C/a) was stronger than that during daytime (0.0004 °C/a). The difference between day and night temperature (DIF) was decreasing. (2) The seasonal changes in LST and DIF in the Qinling-Daba Mountains were significant, and the spatial distribution of their average values in the summer was slightly larger and fluctuated more than in the other seasons. (3) Elevation was the main driving factor affecting the spatial distribution of LST, with the contribution scores of 62.9% in the daytime and 92.7% in the nighttime. The controlling effects of these factors were generally stronger in the nighttime than in the daytime. (4) Nighttime elevation had the strongest interaction with precipitation (contribution score of 95%), while daytime elevation had the strongest interaction with albedo (contribution rate of 83%). We revealed the temporal and spatial variation in LST in the Qinling-Daba Mountains since 2000 and explored the main driving factors involved, thereby improving our understanding of LST changes in the Qinling-Daba Mountains. This study can provide a scientific basis for distinguishing dominant drivers of LST dynamics in the Qinling-Daba Mountains.

Keywords: land surface temperature; driving factors; spatiotemporal differentiation; optimal parameter geographic detector; Qinling-Daba Mountains

Citation: Xi, M.; Zhang, W.; Li, W.; Liu, H.; Zheng, H. Distinguishing Dominant Drivers on LST Dynamics in the Qinling-Daba Mountains in Central China from 2000 to 2020. *Remote Sens.* **2023**, *15*, 878. https://doi.org/10.3390/rs15040878

Academic Editor: Pradeep Wagle

Received: 27 December 2022
Revised: 30 January 2023
Accepted: 3 February 2023
Published: 5 February 2023

1. Introduction

Since the industrial age, the average global land surface temperature (LST) has been increasing rapidly, and climate warming has become a key issue of widespread concern [1,2]. Research shows that, from 1980 to 2012, the global LST showed a linear upward trend, with a total increase of 0.85 °C [3]. According to the Blue Book on Climate Change in China (2019) released by the China Meteorological Administration, from 1951 to 2018, the average annual temperature in China increased by 0.24 °C per decade, a significantly higher increase than the global average during the same period [4,5]. However, in the context of current global climate change, related studies have mostly focused on air temperature [6,7]. Carrying out research on the spatiotemporal differentiation of LST from multi-time series [8,9], and further quantifying the interaction between LST and various driving factors [10,11], can more directly reflect the spatiotemporal differentiation characteristics of LST on the earth's land surface under global warming. Mitigating and adapting to LST changes [9], as well as monitoring agriculture and forestry [12], and urban heat (cold) island effect evaluation and optimization are of great significance [13].

LST is not only an important driving factor in land-atmosphere energy exchange and energy flux control processes [8,14], but is also a key parameter in surface energy budget and water cycle processes at the regional and global scales [15]. The degree of response of various geographical factors to the change in LST also shows a high degree of heterogeneity [4,16]. Some researchers have found that the spatial difference in LST is mainly related to the dynamic changes in the Earth's effective radiation [9]. Temperature change has been shown to be the direct factor leading to changes in LST [8,17], in addition to other important factors, including terrain factors [14,17], the underlying surface [18], and vegetation growth status [19,20]. Previous studies have mostly focused on the relationship between LST and land use and cover changes [21], vegetation changes [22], climatic factors [5], elevation [17], and slope and aspect [23]. However, the relationship between LST and geographic factors, such as albedo, relative humidity and cloud cover, still needs to be further explored [24,25]. In addition, in terms of spatial interaction, most studies have focused on the nonlinear spatial relationship between single or multiple factors and LST [10,26]. Therefore, quantitative analysis of the relationship between LST and multiple factors is the focus of current research on the ecological surface environment under climate change [10,19,27].

There are certain differences in the natural geographical environment of different surface layers on different spatial scales, and the heterogeneity of topography and climate is even more common [28,29]. At present, large-scale LST research mostly explores the spatial heterogeneity of LST globally or nationally from a macro perspective [11]. However, due to the large east–west span of China and the complex natural geographical environment of some mountainous areas, there are often differences in the heterogeneity at different spatial scales [8]. However, studies on China's small-scale LST are mostly focused on urban areas with intensive economic activities [18,27], as well as on ecologically fragile areas, such as the Tibetan Plateau [14], Loess Plateau [30], and Dongting Lake Basin [31]. The Qinling-Daba Mountains are located in the transition zone between the north sub-tropical and warm temperate zones in China, that is, in the north–south transition zone. They play an important role in China's climate, geography, and hydrology [32]. Due to the influence of many factors, such as special geographical location, complex terrain conditions, and mountain climate, LST significantly differs between the north and the south [33]. Previous studies also focused on the spatiotemporal variation characteristics of LST in the Qinling-Daba Mountains and the boundary between the warm temperate zone and the subtropical zone. However, studies on LST have rarely investigated the natural boundaries of geography and climate between north and south China, and the important ecological corridor of the Qinling-Daba Mountains as a whole region and the internal mechanism of LST and related driving factors still needs to be explored [7]. In addition, the existing meteorological observation points are mostly concentrated in urban areas, whereas the mountainous stations are sparsely distributed and are easily affected by terrain and other factors. It is difficult to further capture the region's overall response to climate change [34]. The introduction of high-precision remote sensing data into the study of the Qinling-Daba Mountains provides certain conditions for the quantitative study of LST in the region.

In this study, based on the remote sensing data of LST in the Qinling-Daba Mountains from 2000 to 2020, we analyzed the temporal and spatial evolution characteristics of daytime and nighttime LST of this region in different temporal and spatial dimensions. The OPGD model was further used to quantitatively analyze the multi-factor interaction between LST and various driving factors, such as precipitation (PRE), cloud cover, wind speed (Ws), relative humidity (RH), albedo, solar radiation (SR), elevation, slope, aspect, land use and land cover change (LUCC), NDVI, and vegetation type. It is helpful to understand the characteristics of LST variation particular to a mountainous environment, to provide a theoretical basis for climate change and local environmental monitoring in the Qinling-

Daba Mountains, along with providing new evidence to define the boundary between the warm temperate and subtropical zones in the north and south of China. For these reasons, the specific objectives of this study are: (1) to understand the interannual and seasonal variation of LST in the Qinling-Daba Mountains, an ecologically fragile area; (2) to explore the main driving factors affecting the spatial variation pattern of LST in the Qinling-Daba Mountains; and (3) to determine how the interaction with various driving factors affects LST in a complex geographical environment, and further analyze the impact of the optimal range of each driving factor on LST.

2. Materials and Methods

2.1. Study Area

The Qinling-Daba Mountains are located in central China, between 30° and 36° N and 102° and 114° E (Figure 1). The area is a watershed of the Yangtze River-Yellow River Basin and the main area of China's north–south transition zone. It spans six provinces and cities, namely Henan, Shaanxi, Gansu, Sichuan, Hubei, and Chongqing. The terrain gradually decreases from west to east, with complex and diverse geomorphology and landforms [35]. This area is located in the transition zone between the warm temperate and northern subtropical zones, and the climate difference between the north and the south is large. The air temperature and precipitation rate show a decreasing trend from south to north. The Qinling Mountains are dominated by warm temperate deciduous broad-leaved forests, while the Daba Mountains are dominated by north subtropical evergreen-deciduous broad-leaved mixed forests. It is a north–south transition zone in terms of human society, geography, climate, and biology, and is also a sensitive area for climate change and one of the ecologically vulnerable areas in China [36].

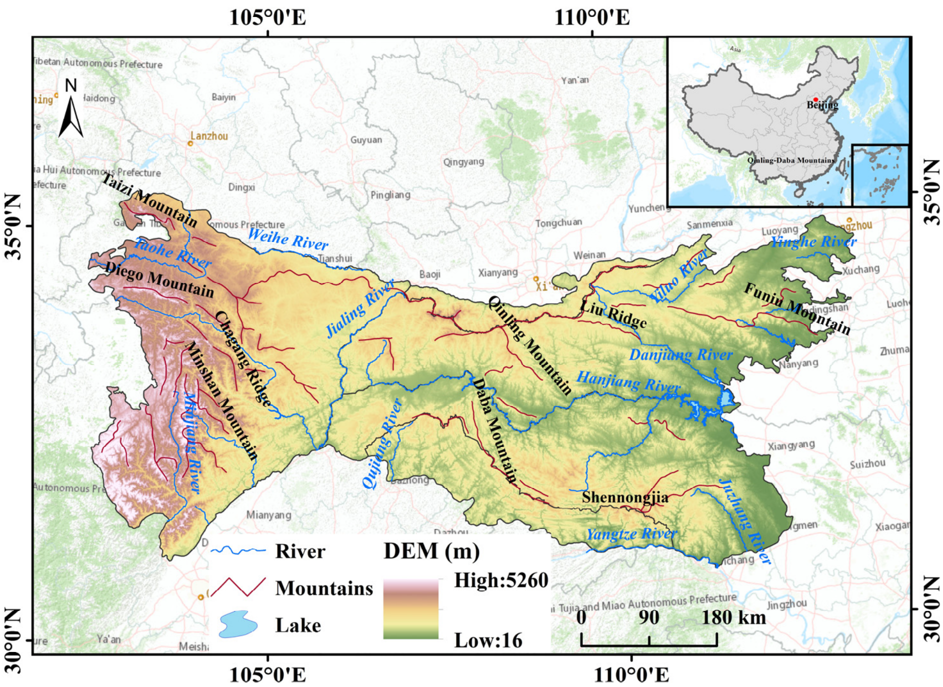

Figure 1. Location of the Qinling-Daba Mountains.

2.2. Data Sources

2.2.1. TRIMS LST

The LST data products were obtained from the National Qinghai-Tibet Plateau Scientific Data Center (http://data.tpdc.ac.cn, accessed on 26 June 2022) with a spatial resolution of 1 km. The principle underlying the generation of this dataset is based on the decomposition model of the LST time series, and utilizes a novel reanalysis and thermal infrared remote sensing data merging (RTM) method to reconstruct the 1-km all-weather LST. The main input data of the method are Terra/Aqua MODIS LST products and GLDAS data, and auxiliary data include NDVI and albedo provided by satellite remote sensing. This dataset utilizes high-frequency components, low-frequency components, and spatial correlation of LSTs, provided by satellite thermal infrared remote sensing and reanalysis data, to reconstruct a high-quality Thermal and Reanalysis Integrating Moderate-resolution Spatial-seamless LST (TRIMS LST) dataset [37], which effectively solves the spatial mismatch problem in the MODIS LST and reanalysis LST datasets. The time span of the selected TRIMS LST data was 2000–2020, and the daytime and nighttime data were unified to 12:30 (local solar time) and 01:00 (local solar time), respectively. Many studies have verified that TRIMS or MODIS daytime and nighttime clear-sky retrievals can be used to calculate the monthly or annual mean LST. Based on previous studies, the TRIMS LST data pre-processing, including the daytime and nighttime LSTs, were averaged to yield the monthly mean LST, and thus the annual mean LST. Each season had 3 months: spring (March, April, and May), summer (June, July, and August), autumn (September, October, and November), and winter (December, January, and February) [38,39]. The data were also divided by season to analyze the spatiotemporal distribution characteristics of annual and quarterly LSTs.

2.2.2. Supplementary Data

The LTDR NDVI dataset was obtained from the National Aeronautics and Space Administration (NASA) (http://ltdr.nascom.nasa.gov, accessed on 26 June 2022) and was the latest dataset for the AVHRR sensor, which is characterized by a long time series. The meteorological data included precipitation, RH, albedo, Ws, SR and cloud cover. Of these, precipitation, RH, SR and Ws data were obtained from the National Qinghai-Tibet Plateau Scientific Data Center (http://data.tpdc.ac.cn, accessed on 26 June 2022) [40,41]. Cloud cover and snowfall were obtained from ERA5 reanalysis data (https://cds.climate.copernicus.eu, accessed on 26 June 2022) with a spatial resolution of $0.01° \times 0.01°$ and a temporal resolution of 1 h. The terrain data was the SRTM 90 m DEM product, which was obtained from the geospatial data cloud (http://www.gscloud.cn, accessed on 26 June 2022), and the aspect and slope data were obtained after processing. The vegetation data was 1:1 million raster data obtained from the Resource and Environmental Science Data Center of the Chinese Academy of Sciences (http://www.resdc.cn, accessed on 26 June 2022), and it showed that the study area included broad-leaved forests, coniferous forests, shrubs, grasses, meadows, cultivated vegetation, and other vegetation types. The land cover data was obtained from GlobeLand30, a 30 m spatial resolution global land cover dataset developed by the National Basic Geographic Information Center (http://www.globallandcover.com, accessed on 26 June 2022) [42].

2.3. Research Methodology

2.3.1. Analysis of the LST Time Series Trend

The trend analysis adopts a one-variable linear regression analysis method, which can be used to simulate the changing trend of different pixels [43]. This method can reduce the impact of accidental factors on LST and accurately reflect the long-term LST change trend [44]. Therefore, this method was used to simulate and analyze the interannual and seasonal trends of LST in the Qinling-Daba Mountains using Equation (1):

$$Slope = \frac{n\sum_{i=1}^{n}(i \times LST_i) - \sum_{i=1}^{n} i \times \sum_{i=1}^{n} LST_i}{n\sum_{i=1}^{n} i^2 - \left(\sum_{i=1}^{n} i\right)^2} \tag{1}$$

where *Slope* is the change trend of LST, i is the number of years, n is the length of the LST time series, and LST_i is the average LST in the ith year; here, n = 21. A positive slope indicates an increase in LST (warming), while a negative slope indicates a decrease in

LST (cooling). The F test was used to determine the significance of the trend using the following equations:

$$F = \frac{S_R}{S_E/(n-2)} \quad (2)$$

$$S_R = \sum_{i=1}^{n} (\hat{y}_i - \overline{y})^2 \quad (3)$$

$$S_E = \sum_{i=1}^{n} (y_i - \hat{y}_i)^2 \quad (4)$$

where S_R and S_E are the error sum of squares and regression sum of squares, respectively, $\hat{y}_i$ is the regression value, $\overline{y}$ is the average LST value throughout the 21 years, and y_i is the actual observed LST value in the *i*th year. Combined with the F test results, the change trend was divided into six grades: extremely significant warming (*Slope* > 0, $p < 0.01$), significant warming (*Slope* > 0, $0.01 < p < 0.05$), insignificant warming (*Slope* > 0, $p > 0.05$), extremely significant cooling (*Slope* < 0, $p < 0.01$), significant cooling (*Slope* < 0, $0.01 < p < 0.05$), and insignificant cooling (*Slope* < 0, $p > 0.05$).

2.3.2. Optimal Parameter Geographic Detector (OPGD)

(1) Variable selection. We used correlation analysis to study the correlation between LST and the independent variables, and selected the variance inflation factor (VIF) method to determine the collinearity of all independent variables (Figure S1 and Table S1). The VIF values of elevation and SR were still higher than the other variables after screening, but they were all less than 10, indicating that there was no strong collinear relationship with other driving factors. Therefore, the precipitation (X1), cloud cover (X2), Ws (X3), RH (X4), albedo (X5), SR (X6), elevation (X7), slope (X8), aspect (X9), NDVI (X10), vegetation types (X11), and LUCC (X12) were incorporated into the OPGD model as driving factors.

(2) Optimal parameter selection. The OPGD model is a quantitative method used to detect spatial heterogeneity and reveal the driving forces behind it [45]. Determining the optimal scale of spatial hierarchical heterogeneity through spatial data discretization is a key point in the use of the OPGD model. Here, methods, such as equal breaks, natural breaks, quantile breaks, geometric breaks, standard and deviation breaks, were compared. The number of levels was selected to filter out the optimal parameters for the analysis in order to carry out the LST driving factor correlation analysis.

(3) Factor Detector. To detect the spatial differentiation of LST (Y) and the extent to which the driving factors (X) explained the spatial differentiation of Y, the factor detector revealed the relative importance of the explanatory variables through q statistics. Among them, X_1, X_2, X_3, X_4, X_5, X_6, X_7, X_8, X_9, and X_{10} refer to the average annual temperature, precipitation, cloud cover, NDVI, elevation, aspect, slope, LUCC, vegetation type, and snowfall, respectively. The q value of each explanatory variable was calculated using Equation (5):

$$q = 1 - \frac{\sum_{i=1}^{L} N_i \sigma_i^2}{N\sigma^2} = 1 - \frac{SSW}{SST} \quad (5)$$

where $i = 1, 2, \ldots, L$ are the strata of Y or X, i.e., classification or partition; σ_i^2 and σ^2 are the variances of units in local strata i and global strata, respectively; N_i and N are the numbers of units in local strata i and global strata, respectively; SSW is the within sum of squares; and SST is the total sum of squares. The q value ranges from 0 to 1; the higher the q value, the stronger the explanatory power.

(4) Risk Detector. This is used to determine whether there is a significant difference in the attribute mean between two sub-regions. The sub-region with a higher mean value has a higher LST value and can be used to determine which areas are high-

temperature areas of the LST. The risk detector was tested with the t-test and calculated by Equation (6):

$$t = \frac{\overline{Y}_{i=1} - \overline{Y}_{i=2}}{\left[\frac{Var\left(\overline{Y}_{i=1}\right)}{n_{i=1}} + \frac{Var\left(\overline{Y}_{i=2}\right)}{n_{i=2}}\right]} \tag{6}$$

where $\overline{Y}_i$ is the average value of the observations of the subregion i, n_i is the number of observations, and *Var* is the variance.

(5) Interaction Detector. While considering a single influencing factor, the interaction between different drivers was identified, that is, the explanatory power of the combined (enhanced or weakened) and independent effects of the drivers on LST was assessed. Five types of interactions between the two factors were observed and are shown in Table 1.

Table 1. Types of interactions between two factors.

Interaction	Judgment Criteria
$q(X_1 \cap X_2) < Min(q(X_1), q(X_2))$	Nonlinear weaken
$Min(q(X_1), q(X_2)) < q(X_1 \cap X_2) < Max(q(X_1), q(X_2))$	Univariate weaken
$q(X_1 \cap X_2) > Max(q(X_1), q(X_2))$	Bivariate enhance
$q(X_1 \cap X_2) = q(X_1) + q(X_2)$	Independent
$q(X_1 \cap X_2) > q(X_1) + q(X_2)$	Nonlinear enhance

3. Results

3.1. Spatiotemporal Variation Characteristics of LST

The average annual LST had obvious spatial differentiation patterns in the Qinling-Daba Mountains from 2000 to 2020, and the overall distribution characteristics were high in the east and low in the west (Figure 2). The low-value areas of the average annual LST were mainly concentrated in the areas west of the Jialing River, and the high-value areas were distributed on both sides of the Hanjiang River.

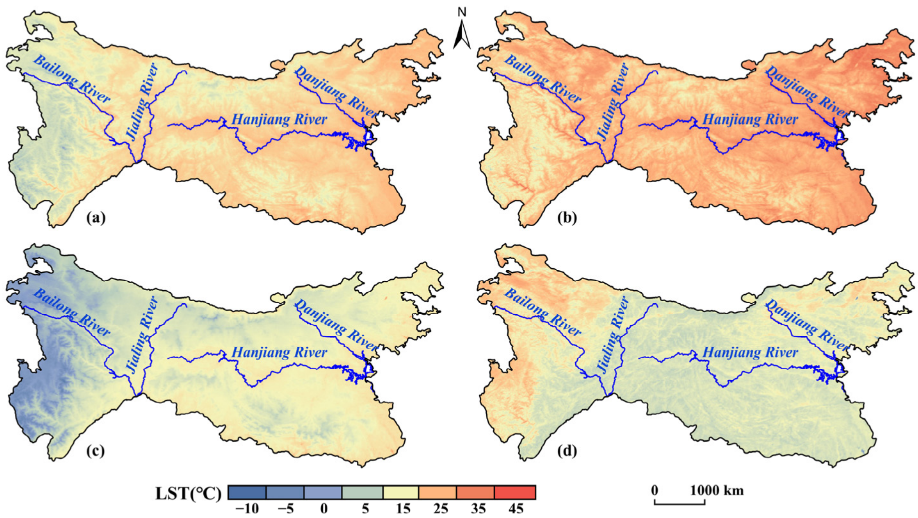

Figure 2. Spatial distribution of LST in the Qinling-Daba Mountains from 2000 to 2020: (**a**) average annual LST; (**b**) daytime LST; (**c**) nighttime LST; and (**d**) DIF.

Among them, the average annual LST was slightly lower south of the Hanjiang River and near the ridgeline of the Daba Mountains and the Micang Mountains. The high-value areas were mainly concentrated in the east of the Daba Mountains, while north of the Hanjiang River, the high-value areas were mainly concentrated in the northeast of the Qinling Mountains. The low-value areas of the average annual daytime LST were mainly located in the mountainous areas with higher elevation, such as the Honggang Mountains, Minshan Mountains, Yanggong Mountains and Chagangling Mountains to the west of the Jialing River, and the main ridgelines of the Qinling Mountains and Daba Mountains; the high-value areas were mainly located in the northeastern part of the Qinling Mountains. The spatial differentiation characteristics of the average annual nighttime LST were similar to the average annual LST, and the nighttime LST in the areas west of the Jialing River was lower; the high-value areas were mainly located on both sides of the Hanjiang River and in the south and east of the Daba Mountains. In addition, the DIF in the Qinling-Daba Mountains was high in the middle of the region and low in the east and west. The high-value areas were mainly located around the mountains with higher elevation, mostly concentrated in the West Qinling Mountains, west of the Jialing River, and a small amount in the northeast of the Qinling Mountains.

The average annual LST showed an increasing trend year by year (0.034 °C/a) in the Qinling-Daba Mountains from 2000 to 2020, with the most obvious rise in LST at nighttime (0.066 °C/a). The increasing trend of daytime LST was not significant (0.0004 °C/a) (Figure 3). From the perspective of inter-annual variation, the average annual LST peaked at 19.14 °C in 2002, and dropped to a minimum in 2012 (16.89 °C). The average daytime LST peaked at 25.87 °C in 2013 and dropped to its lowest (23.16 °C) in 2012; while the average nighttime LST peaked at 12.67 °C in 2018 and reached its minimum of 9.70 °C in 2001. Moreover, the DIF showed a decreasing trend year by year, with a decreasing rate of 0.065 °C/a. This is thought to be due to the interruption of global warming from 1998 to 2012. The warming trend was significantly lower during this time than in previous decades, and the warming gradually disappeared in the short and medium term after 2014. At the same time, in the winter of 2012, the temperature was lower and the snowfall increased, and the large-scale snow accumulation led to the enhancement of surface albedo. In 2018, the western Pacific subtropical high was extremely abnormal, crossing the area at almost 40° north latitude. Under the influence of the abnormal subtropical high, the LST in 2018 was higher than throughout the historical period.

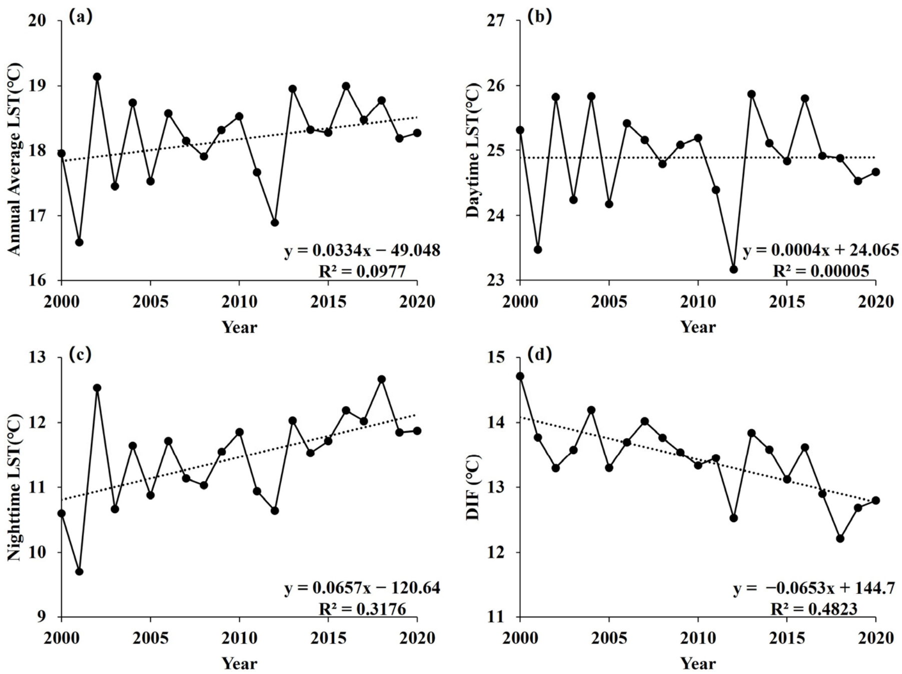

Figure 3. Interannual trends of LST in the Qinling-Daba Mountains from 2000 to 2020: (**a**) annual average LST; (**b**) daytime LST; (**c**) nighttime LST; and (**d**) DIF.

The complex geomorphological pattern of the Qinling-Daba Mountains is the reason for the obvious regional differences in the spatiotemporal distribution of interannual LST changes. To further explore the pattern and regional differences in LST changes among different regions, we analyzed the average annual LST change trends in the Qinling-Daba Mountains from 2000 to 2020 (Figure 4). Most areas showed a warming trend, and the overall rate of LST warming gradually decreased on both sides, with the Hanjiang River as the dividing line. Further analysis of daytime and nighttime changes in the interannual LST showed that the warming and cooling trends during the daytime were significantly higher than those during the nighttime, and the warming and cooling trends of interannual LST were most affected by daytime changes. Furthermore, human activities, solar radiation intensity, and sunshine time changes were the dominant factors affecting daytime warming.

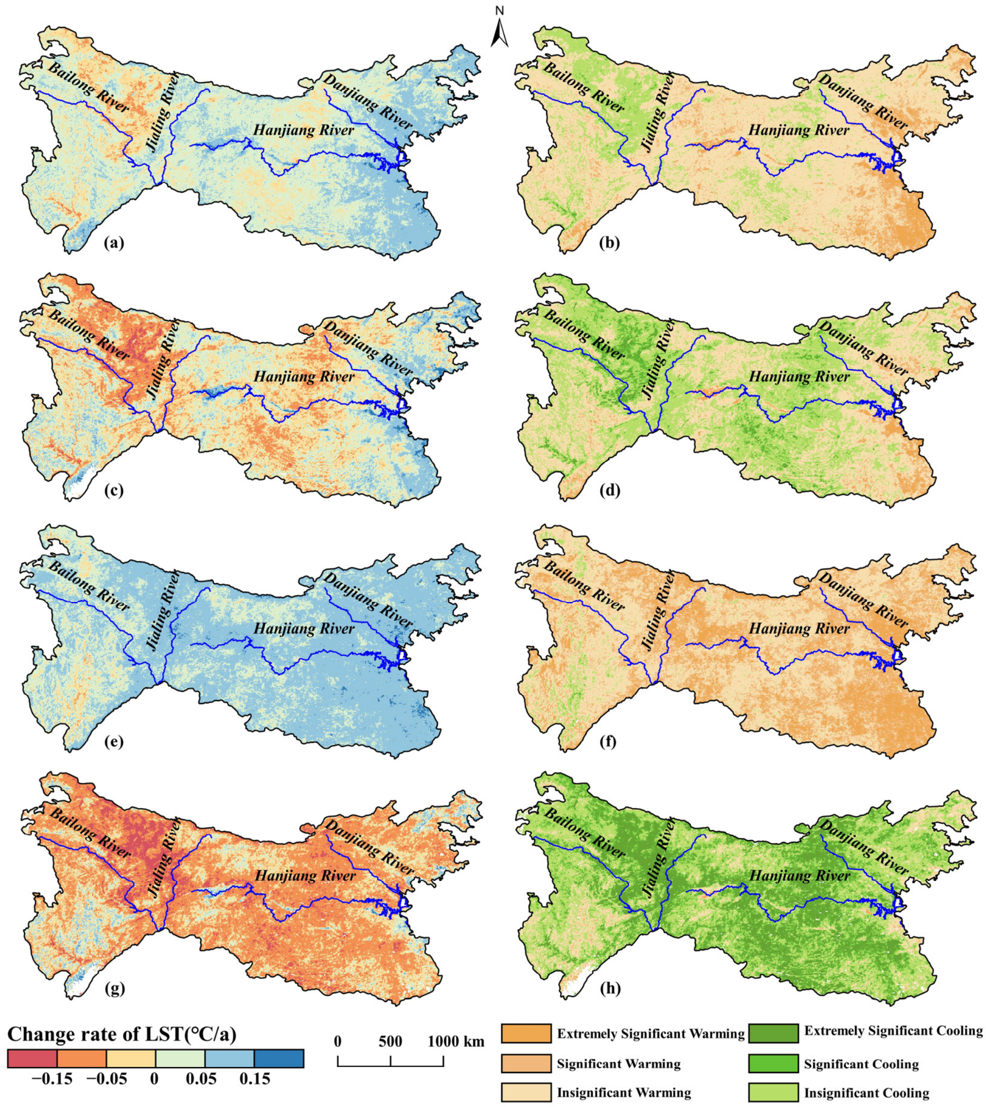

Figure 4. The interseasonal variability rates (slope) and trend significance of LST in the Qinling-Daba Mountains from 2000 to 2020: (**a**,**b**) spatial distributions of slope and trend significance for the average annual LST; (**c**,**d**) spatial distributions of slope and trend significance for the daytime LST; (**e**,**f**) spatial distributions of the slope and trend significance for the nighttime LST; and (**g**,**h**) spatial distributions of the slope and trend significance for DIF.

3.2. Seasonal Spatiotemporal Variation Characteristics of LST

Our results showed that the variation in LST had significant seasonal differences. We analyzed the spatial distribution and its variation trend in different seasons and illustrate the temporal and spatial variation patterns of LST in a more detailed manner in Figure 5. From highest to lowest, the seasonal LSTs and DIFs in the Qinling-Daba Mountains from 2000 to 2020 followed the trend of summer > spring > autumn > winter. The DIF was the lowest in winter mainly because of the short sunshine duration and high snow and ice coverage, and the specific heat characteristics of ice and snow decrease LST fluctuation.

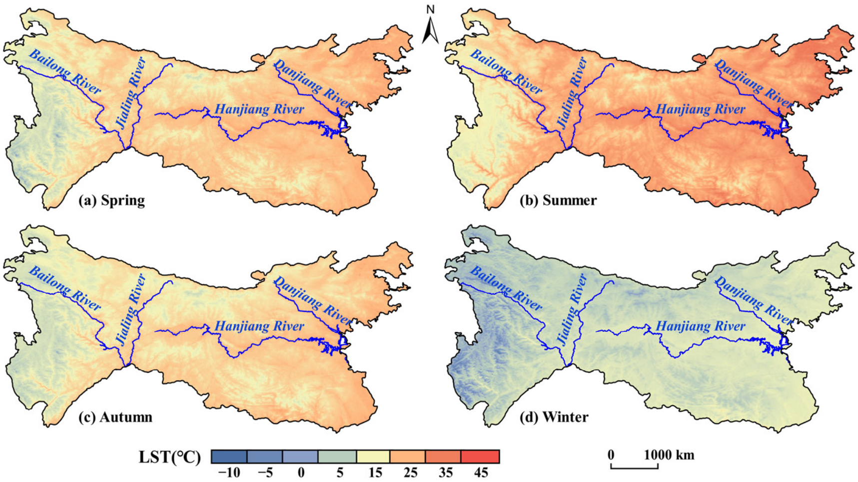

Figure 5. Spatial distribution of multiyear mean daytime and nighttime LST in spring (**a**); summer (**b**); autumn (**c**); and winter (**d**) in the Qinling-Daba Mountains from 2000 to 2020.

Furthermore, we also found significant differences between seasonal LST variation trends in the Qinling-Daba Mountains (Figures 6 and 7). The LST change rate in the summer (0.102 °C·a^{-1}) was much higher than that of other seasonal and interannual LSTs, and 78.8% of the study area showed a warming trend, which was particularly pronounced in the Hanjiang, Yinghe, and Shahe rivers. The LST change rate in the spring was the second highest (0.417 °C·a^{-1}), and the area with a greater variation in LST was the Danjiangkou Reservoir. The amplitude of LST variation in autumn was relatively small (0.013 °C·a^{-1}). This is due to the fact that with global warming, the delay of vegetation phenology and the extension of the growing season promote changes in vegetation greenness and slow down the upward trend of LST. The amplitude of LST variability in winter was essentially the same as that in autumn. Winter was dominated by cooling, with the largest amplitude of cooling recorded in the Taizishan Mountains. The winter LST reached its minimum in 2011, which may be the result of the strong East Asian winter monsoon and the La Niña influence of the winter Pacific.

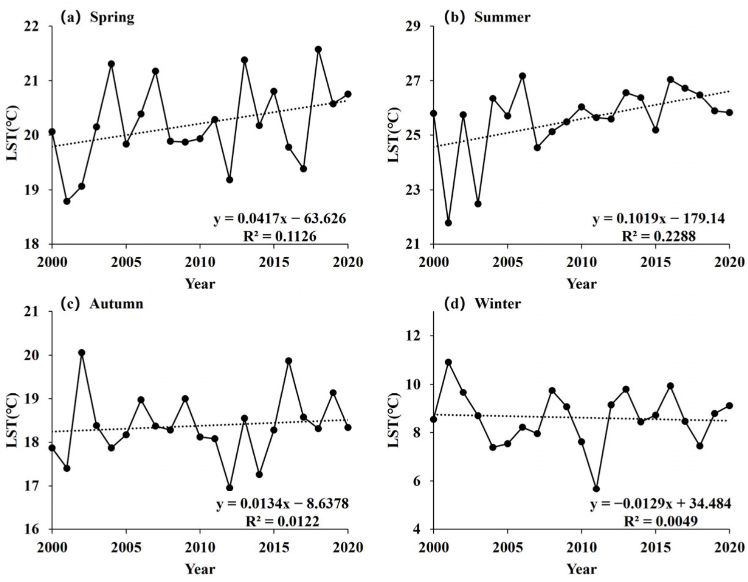

Figure 6. Interannual change trends in mean daytime and nighttime LST in spring (**a**); summer (**b**); autumn (**c**); and winter (**d**) in the Qinling-Daba Mountains from 2000 to 2020.

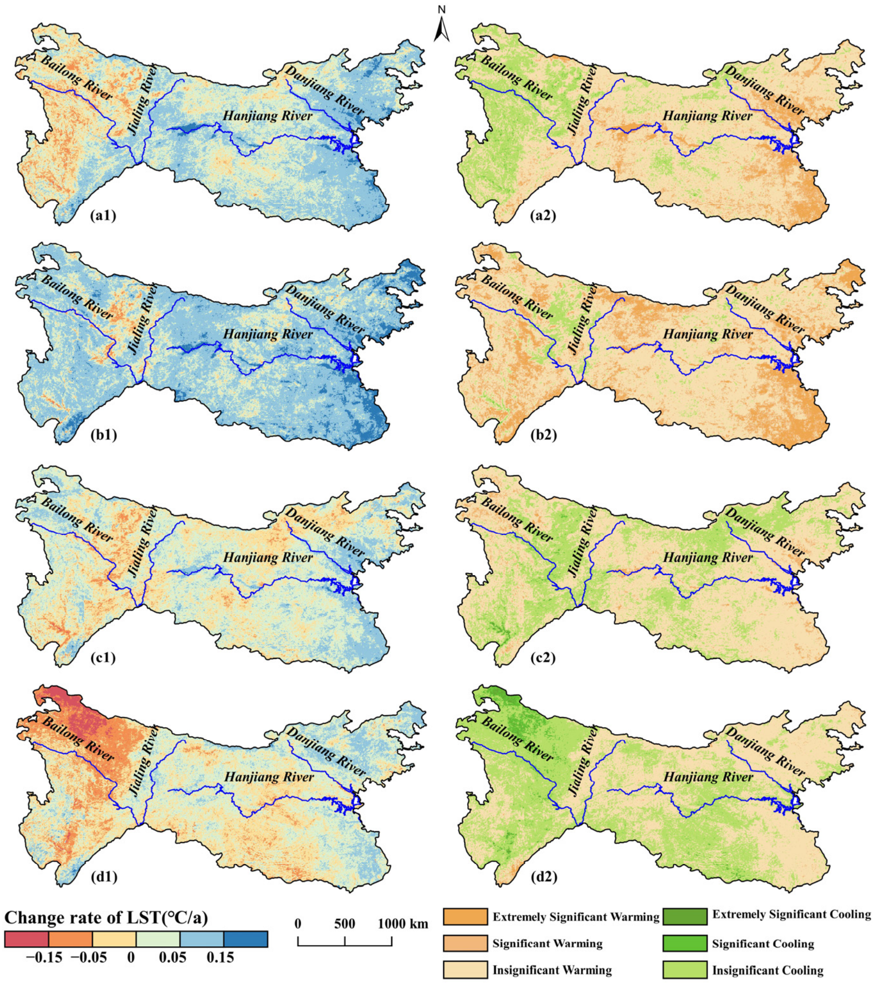

Figure 7. The interseasonal variability rates (slope) and trend significance of LST in spring (**a**); summer (**b**); autumn (**c**); and winter (**d**) in the Qinling-Daba Mountains from 2000 to 2020. (**a1**–**d1**) show the spatial distributions of the slopes in the four seasons; and (**a2**–**d2**) show the spatial distributions of the trend significance in the four seasons.

3.3. Impacts of Driving Factors on LST Spatial Distribution

3.3.1. Contribution from Individual Factors

To explore the LST spatial distribution pattern, we used factor detectors to analyze the contribution of selected driving factors to LST. The q values of each factor are shown in Table 2, and all q values passed the significance test ($p < 0.01$). The nighttime q values of each driving factor were higher than the daytime values, and these differences revealed that the changing mechanism of LST is more complex in the daytime than in the nighttime. From highest to lowest, the q values of the influence of each driving factor on the spatial distribution of daytime and nighttime LST were ranked as follows: $X_7 > X_5 > X_{11} > X_2 > X_8 > X_{12} > X_6 > X_4 > X_1 > X_{10} > X_3 > X_9$; $X_7 > X_6 > X_1 > X_4 > X_{11} > X_5 > X_{10} > X_2 > X_3 > X_8 > X_{12} > X_9$, respectively. The factor detection results showed that the q value of elevation was the largest in both the daytime and nighttime, and elevation was the main driving factor affecting the spatial distribution of LST. The influence of the daytime albedo was the second-largest, and albedo directly affected the available energy of the surface, which in turn had a direct impact on LST. However, the influence of albedo at nighttime was less than that of solar radiation. There was no solar radiation at nighttime, but there was ground radiation. When the earth's surface absorbs solar radiation, it transmits most of the energy to the atmosphere in the form of radiation. The contribution of a single factor of aspect was less than 10%, and its influence on the spatial distribution of LST was small.

Table 2. The *q* values of single factors for daytime and nighttime LST.

	X_1	X_2	X_3	X_4	X_5	X_6	X_7	X_8	X_9	X_{10}	X_{11}	X_{10}	X_{12}
Daytime	0.085	0.268	0.058	0.122	0.306	0.128	0.629	0.234	0.003	0.081	0.276	0.081	0.167
Nighttime	0.358	0.133	0.086	0.352	0.210	0.605	0.927	0.074	0.002	0.178	0.248	0.178	0.062

Notes: X_1 is Precipitation, X_2 is Cloud cover, X_3 is Ws, X_4 is RH, X_5 is Albedo, X_6 is SR, X_7 is Elevation, X_8 is Slope, X_9 is Aspect, X_{10} is NDVI, X_{11} is vegetation type, X_{12} is LUCC.

3.3.2. The Dominant Factors of the Spatial Differentiation of LST Change between Geomorphic Types

The geomorphology of the Qinling-Daba Mountains is complex and diverse, and the landform fluctuates greatly, resulting in a diversity of climate, plants, and soil. The differences in geomorphic types lead to large differences in the explanatory power of each driving factor for the spatial differentiation of LST (Figure 8 and Table 3). The same driving factors had different effects on LST in different geomorphic types. Albedo was the main driving factor determining the spatial variation of daytime LST in plains, platforms, hills, and extremely large relief landforms. Driving factors, such as elevation, NDVI and cloud cover, also had a greater impact on the daytime LST of plains, platforms and hills. In small, medium and large relief landforms, the main driving factor was elevation, which contributed significantly more to the spatial distribution of daytime LST than other factors. However, in extremely large relief landforms, the influence of RH and SR on daytime LST was similar to that of albedo. In addition, there were also certain differences in the influence of each driving factor on the daytime and nighttime LSTs of different geomorphic types, and the *q* value at nighttime was greater than that during the daytime. In terms of geomorphic types, elevation was the main factor affecting nighttime LST, and the *q* value was significantly higher than other driving factors. Slope and NDVI had less influence. In extremely large relief landforms, RH played a leading role, with the largest *q* value (0.7), and the effect of elevation was slightly smaller, with a *q* value of 0.32. Slope, aspect and LUCC were not among the main driving factors affecting LST.

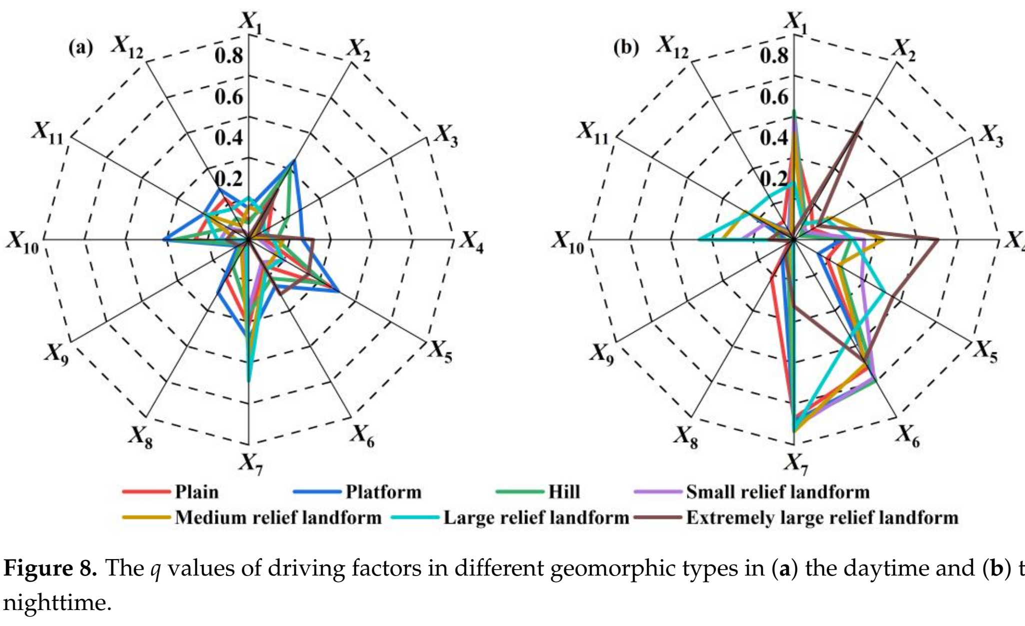

Figure 8. The *q* values of driving factors in different geomorphic types in (**a**) the daytime and (**b**) the nighttime.

Table 3. Main influencing factors and corresponding q values in different geomorphic types for daytime and nighttime LST.

Geomorphic Types		Influencing Factors (q)			
Daytime	Plain	Albedo (0.46)	Elevation (0.42)	NDVI (0.26)	Cloud cover (0.24)
	Platform	Albedo (0.50)	Elevation (0.48)	Cloud cover (0.44)	NDVI (0.41)
	Hill	Albedo (0.42)	Cloud cover (0.40)	Elevation (0.36)	NDVI (0.36)
	Small relief landform	Elevation (0.34)	Cloud cover (0.21)	Albedo (0.20)	NDVI (0.14)
	Medium relief landform	Elevation (0.57)	Veg (0.25)	RH (0.17)	SR (0.16)
	Large relief landform	Elevation (0.69)	Veg (0.24)	Pre (0.21)	Albedo (0.19)
	Extremely large relief landform	Albedo (0.34)	RH (0.313)	SR (0.307)	Cloud cover (0.28)
Nighttime	Plain	Elevation (0.87)	SR (0.72)	Pre (0.48)	RH (0.24)
	Platform	Elevation (0.88)	SR (0.78)	Pre (0.53)	RH (0.23)
	Hill	Elevation (0.89)	SR (0.79)	Pre (0.63)	RH (0.28)
	Small relief landform	Elevation (0.91)	SR (0.78)	Pre (0.59)	RH (0.38)
	Medium relief landform	Elevation (0.93)	SR (0.70)	Pre (0.52)	RH (0.43)
	Large relief landform	Elevation (0.93)	SR (0.55)	Albedo (0.51)	NDVI (0.46)
	Extremely large relief landform	RH (0.70)	SR (0.68)	Cloud cover (0.66)	Albedo (0.56)

3.3.3. Driving Factors Indicate Function

Besides identifying significant differences between the driving factors, risk detection can also help identify the optimal range at which each factor can significantly affect the LST, and pass the statistical significance test at the 95% confidence level (Table 4, Figures S2 and S3). This pattern is evident from the optimal range results showing that, when LST was at its maximum, the types and optimal ranges of the driving factors were roughly the same during the daytime and the nighttime. With the increase in elevation, cloud cover, and slope, the LST gradually decreased in the daytime and nighttime, and the average LST reached its maximum, within the ranges of 54.2–484 m, 53.7–60.5%, and 0–1.65°. The daytime LST variation in the optimal intervals of Ws, RH and aspect had little difference, but at nighttime, due to the cooling effect and the reduction of transpiration, the fluctuation range of wind speed and relative humidity in each optimal interval increased. Precipitation, albedo, SR, and NDVI had a curvilinear interaction relationship with LST. With the increase in precipitation, albedo, SR and NDVI, the LST presented a distribution feature that increased first and then decreased. In the ranges of 867–936 mm, 7.95–10.2%, 148–156 W/m^2 and 0.37–0.41 for precipitation, albedo, SR, and NDVI, respectively, LST reached its maximum during the daytime. In the ranges of 951–1060 mm, 5.24–6.8%, and 0.52–0.55 for precipitation, albedo, and NDVI, respectively, LST was at its highest during the nighttime. When the LUCC and vegetation types were different, the LST was obviously different and showed a fluctuating trend. When the LUCC type was an artificial surface, the daytime LST reached the maximum value, which was related to the low thermal conductivity and rapid heating of the artificial surface. The LST of the water area was the highest at nighttime, which was related to the thermal insulation effect of the water, natural convection inside the water body, and sufficient water on the surface for evaporation, which made the water area cool down slowly.

Table 4. Type or range of the influence factors at maximum LST.

Factors	Type or Range		LST/°C	
	Daytime	Nighttime	Daytime	Nighttime
Pre/mm	867–936	951–1060	26.48	15.43
Cloud cover/%	53.7–56.4	53.7–60.5	31.49	14.32
Ws/m·s^{-1}	2.21–2.52	0.93–1.28	28.41	13.97
RH/%	78.8–80.1	84.6–88.5	26.44	14.58
Albedo/%	7.95–10.2	05.24–6.8	27.81	12.57
SR/W·m^{-2}	148–156	137–142	26.56	14.46
Elevation/m	54.2–484	54.2–477	30.55	16.88

Table 4. *Cont.*

Factors	Type or Range		LST/°C	
	Daytime	Nighttime	Daytime	Nighttime
Slope/°	0–1.65	0–0.51	28.58	15.25
Aspect	south	southwest	25.07	11.67
NDVI	0.37–0.41	0.52–0.55	27.76	13.34
Vegetation types	Cultivated vegetation	Grass	27.88	13.90
LUCC	Artificial surface	Water body	31.41	15.93

3.3.4. Interaction between the Driving Factors

Interaction detector is mainly used to identify the interactive effects of different driving factors on LST distribution and analyze whether it would enhance or weaken the explanatory power of LST distribution, as well as whether the effects of these driving factors on LST distribution are independent of each other. The q values of the interaction and interaction types are shown in Figure 9. Overall, the interaction q values of most driving factors were higher than the q values of single factors, and the interaction effects of the factors showed a relationship of bivariate and nonlinear enhancement. This indicated that the spatial distribution of LST was the result of a combination of factors, rather than a single factor.

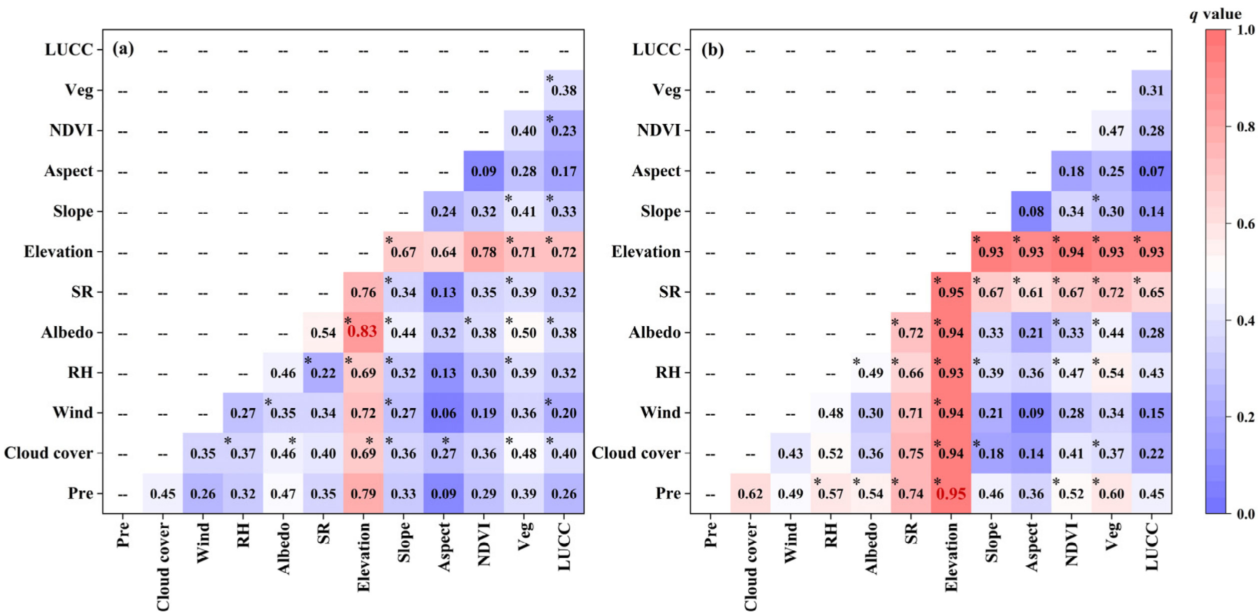

Figure 9. Interaction detection of driving factors in the (**a**) daytime and (**b**) nighttime. Notes: The asterisks indicate that the interaction between the two factors is bivariate enhancement; unmarked indicates that the interaction between the two factors is nonlinear enhancement; "–" indicates no data. The value and color of each box represent the strength of the interaction between the two factors on surface temperature in both horizontal and vertical coordinates; the greater the value, the darker the red color and the stronger the interaction; the lower the value, the darker the purple color and the weaker the interaction.

Similar to the effect of a single factor on LST changes, the interactions of elevation with other factors were significant during both daytime and nighttime. The q values of the interactions of elevation with other driving factors were all greater than 0.9 at nighttime, which again proved that elevation was the main factor driving the spatial distribution of LST. The degree of increase in the q values of the interaction between driving factors during the daytime was higher than that during the nighttime, indicating that daytime interaction had a stronger effect on the spatial distribution of LST. At nighttime, the interaction between elevation and precipitation had the highest q value (0.95), whereas during the daytime, the interaction between elevation and albedo had the highest q value (0.83). We also found great differences between the interaction effect and influence of a single factor on LST. In single factor detection, the q values of aspect, Ws, and NDVI were relatively small. However, the interaction effect of these three factors increased greatly during both the daytime and nighttime. Furthermore, the effects of aspect, Ws, and NDVI on LST changes were mainly reflected in the interaction with other factors. In conclusion, the influence of driving factors on LST is not independent, but their interaction is significant; the influence of multi-factor interaction on LST is not a simple superposition process, but has a bivariate enhancement or nonlinear enhancement.

4. Discussion

The Qinling-Daba Mountains are an important area that divides the north and south of China. As a consequence of the differences in geographical location and climatic conditions, the non-zonal law within the region is particularly significant. The spatial heterogeneity of LST is closely related to factors, such as elevation, aerosol concentration, LUCC, and vegetation coverage [21,24,46,47]. In the present study, we found that elevation was the main driving factor of LST. However, in reality, the effect of terrain on LST is usually not determined by a single terrain factor, and regional differences in LST are often the result of combined effects of multiple terrain factors. Therefore, the actual influence of terrain on LST can be effectively described only by comprehensively considering the influence of terrain factors, such as elevation, slope, and aspect. Furthermore, we found that LST was negatively correlated with elevation, which was similar to the findings of the study carried out in Hangzhou, China, which showed that LST was negatively linearly correlated with elevation [23]. In addition, some researchers have analyzed the impact of terrain factors, underlying surface characteristics, and vegetation growth conditions on the spatial differentiation of the surface thermal environment, considering the differences between day and night [16,18,20]. In this study, we incorporated albedo, wind speed, and relative humidity to the study of LST driving factors. The results show that the impact of albedo on the spatial variation of LST during the daytime is second only to that of elevation, and the increase in albedo reduces the absorption of solar radiation, thereby causing a decrease in LST. The interaction between albedo and elevation during the daytime is the strongest, because albedo and elevation are positively correlated, and high-elevation areas also cause LST to decrease, so the interaction between the two has a greater impact on LST [48]. At nighttime, the interaction between elevation and precipitation is stronger. More precipitation leads to an increase in soil moisture. Changes in soil moisture can cause changes in latent and sensible heat, thereby causing changes in LST [49]. We also found that the impact of static variables (topographic elements) on LST is higher than that of dynamic variables (meteorological elements). This is because topographic factors, as relatively stable elements, directly affect LST through relatively fixed limiting factors, such as elevation decline, shady and sunny slopes, peak and valley topography, and the mountain effect of the Qinling-Daba Mountains, thereby making the change of LST more complicated. Meteorological elements have more indirect effects on LST, which are easily disturbed by other elements and are unstable [50,51].

In general, in terms of driving factors and method choice, many researchers have focused on the interaction between a single factor and LST [14,22]. Although the impact of different driving factors on the spatial differentiation of LST has been studied in detail, it is impossible to compare different driving factors at the same level. Therefore, it is very important to select an effective analysis method to study the impact of various driving factors on LST. However, the currently available methods, such as the spatial error model, spatial lag model, and spatial autocorrelation often ignore the interaction of internal correlation characteristics among various factors in space and thus cannot accurately reflect the heterogeneity between regions [4,52]. As a powerful tool for analyzing spatial variability, the geodetector model breaks through the linear assumption of traditional models and is widely used to study the mechanisms underlying the impact of natural environmental variables. It is also based on nonlinear assumptions, and it is not necessary to know in advance whether the relationship between factors is additive or multiplicative when exploring the interaction relationship. In addition, collinearity can be avoided, and factors can be analyzed regardless of whether they comprise qualitative or quantitative data. In order to improve the accuracy and reliability of the results, we based the present study on the pixel scale, which reflects the spatial distribution characteristics of each driving factor in a more refined manner, to further deepen the microscopic research on the impact of LST, and we used the geodetector model to examine the relationship between LST and various driving factors. Many judgments in the parameter identification of the optimal scale of spatial hierarchical heterogeneity in geodetector are subjective, which leads to biased detection results [53]. Therefore, the present study used the OPGD model to objectively assess the contribution of each driving factor, more accurately identifying the interaction mode and process [54], and scientifically revealing the influence mechanism of various geographical elements on the spatial differentiation of LST. This allowed us to describe and understand the variation characteristics of LST in a complex geographical environment in detail, and has certain reference value for promoting ecological monitoring and ecological environmental protection in the Qinling-Daba Mountains.

Traditional remote sensing data are easily affected by cloud blocking, atmospheric disturbances, and other factors, resulting in large areas of missing data. Due to the complexity of LST on spatiotemporal scales, the problem of missing pixels limits its further application in the study of regional surface thermal environments [55,56]. Currently, the common LST data products include Landsat, Moderate-resolution Imaging Spectroradiometer (MODIS), and Advanced Spaceborne Thermal Emission and Reflection Radiometer (ASTER) [57–59]. Landsat has a long revisit period (16 days) and generally only provides data during the day. If affected by clouds, there may be no data available for several months, which limits the application of Landsat LST datasets [60]. The MODIS LST dataset effectively solves some problems of the Landsat LST dataset. However, because of the lack of effective pixel data, obvious overestimation or underestimation can occur in certain cloudy conditions based on its calculation results [58]. ASTER can provide high-resolution (90 m) LST data, but its widespread application in surface thermal environment research is hindered by high costs and limited data archiving because of the high acquisition cost of ASTER imagery [59]. The TRIMS LST uses the RTM method for synthesis optimization. This method has high accuracy under both clear sky and non-clear sky conditions and effectively solves the spatial mismatch between the MODIS LST and reanalysis LST datasets. Therefore, the present study is conducive to promoting the application of TRIMS LST in the study of surface thermal environments, as well as to exploring the spatiotemporal characteristics and driving factors of the surface thermal environment under real all-weather conditions from a richer time and space dimension.

5. Conclusions

In the present study, based on TRIMS LST, DEM, LUCC, and other data, and using trend analysis methods and the OPGD model, we studied the spatiotemporal patterns of LST change in the Qinling-Daba Mountains from 2000 to 2020, and quantitatively analyzed and discussed the internal relationship between them and various driving factors. This paper mainly constructs a framework for exploring the spatiotemporal differentiation and influencing factors of LST in mountainous areas. After analysis, this method can be extended to other mountainous areas. At the same time, in the study of LST in other mountainous areas, this study provides a reference for the selection of driving factors, such as elevation and albedo, etc. as the primary choices. The main conclusions are as follows:

(1) From 2000 to 2020, the average annual LST in the Qinling-Daba Mountains showed a significant upward trend; the warming area accounted for 82.5% of the total area, while the cooling area accounted for 17.5%. During the study period, both daytime and nighttime LST in the Qinling-Daba Mountains showed an upward trend, but the nighttime warming effect was stronger than that of the daytime, and the difference

between day and night temperature continued to decrease. Meanwhile, the trend of LST changed significantly in different seasons, with the most obvious warming trend in the summer.

(2) Differences in the influence of various driving factors on LST were observed. Among them, elevation was the main factor driving the spatial distribution of LST. Elevation had the greatest explanatory power both in the daytime and nighttime, followed by albedo in the daytime and precipitation in the nighttime, and the explanatory power for LST changes was higher at nighttime than during daytime. The mean LST of different ranges or types of driving factors was different, and the maximum LST corresponded to different ranges or types of drivers.

(3) The interaction analysis found that the impact of driving factors on LST was not independent, but rather the result of a combination of factors. Compared with the influence of a single factor on LST, the interaction effect was quite different. The interaction among driving factors was significant. The effect of multi-factor interaction on LST is not a simple superposition process, but has bivariate enhancement or nonlinear enhancement.

Overall, this study improved our understanding of the variation characteristics of LST in the special mountainous environment, which has certain reference value for mitigating and coping with climate change in the Qinling-Daba Mountains. The results of the study can also provide new evidence for the definition of the boundary between the north and south warm temperate zone and subtropical zone in China.

Supplementary Materials: The following supporting information can be downloaded at: https://www.mdpi.com/article/10.3390/rs15040878/s1, Figure S1: Correlation analysis between all the variables in the (**a**) daytime and (**b**) nighttime; Figure S2: Optimal ranges and tipping points of driving factors that influence daytime LST; Figure S3: Optimal ranges and tipping points of driving factors that influence nighttime LST; Table S1: Correlation analysis between all the variables.

Author Contributions: Conceptualization, M.X., H.Z. and W.Z.; methodology, M.X. and W.Z.; software, W.L. and H.L.; validation, W.L., H.L., W.Z. and M.X.; formal analysis, H.L. and W.Z.; investigation, M.X. and W.Z.; resources, M.X. and H.Z.; data curation, W.Z.; writing—original draft preparation, M.X. and W.Z.; writing—review and editing, H.Z. and M.X.; visualization, W.Z., W.L. and H.L.; supervision, M.X. and H.Z.; project administration, H.Z. and M.X.; funding acquisition, H.Z. The first two authors contributed equally to this work and should be considered co-first authors. All authors have read and agreed to the published version of the manuscript.

Funding: This research was funded by the National Natural Science Foundation of China (grant number 42005102), the Project funded by the Natural Science Foundation of Henan Province (grant number 222300420129), the China Postdoctoral Science Foundation (2021M701054) and the Science and Technology Development Project of Henan Province China (grant number 222102110419).

Data Availability Statement: The land surface temperature data products were obtained from the National Qinghai-Tibet Plateau Scientific Data Center (http://data.tpdc.ac.cn, accessed on 26 June 2022). The NDVI data products was obtained from National Aeronautics and Space Administration (NASA) (http://ltdr.nascom.nasa.gov, accessed on 26 June 2022). Precipitation and average annual temperature data were obtained from the National Qinghai-Tibet Plateau Scientific Data Center (http://data.tpdc.ac.cn, accessed on 26 June 2022). Cloud cover and snowfall were obtained from ERA5 reanalysis data (https://cds.climate.copernicus.eu, accessed on 26 June 2022). The terrain data was the SRTM 90 m DEM product, which was obtained from the geospatial data cloud (http://www.gscloud.cn, accessed on 26 June 2022). The vegetation data was obtained from the Resource and Environmental Science Data Center of the Chinese Academy of Sciences (http://www.resdc.cn, accessed on 26 June 2022). The land cover data was obtained from the National Basic Geographic Information Center (http://www.globallandcover.com, accessed on 26 June 2022).

Acknowledgments: We thank the reviewers who provided valuable comments to improve the paper.

Conflicts of Interest: The authors declare no conflict of interest.

References

1. Eleftheriou, D.; Kiachidis, K.; Kalmintzis, G.; Kalea, A.; Bantasis, C.; Koumadoraki, P.; Spathara, M.E.; Tsolaki, A.; Tzampazidou, M.I.; Gemitzi, A. Determination of annual and seasonal daytime and nighttime trends of MODIS LST over Greece—Climate change implications. *Sci. Total Environ.* **2018**, *616*, 937–947. [CrossRef]
2. Li, Q.; Sun, W.; Huang, B.; Dong, W.; Wang, X.; Zhai, P.; Jones, P. Consistency of global warming trends strengthened since 1880s. *Sci. Bull.* **2020**, *65*, 1709–1712. [CrossRef] [PubMed]
3. Stocker, T.F.; Qin, D.; Plattner, G.K.; Tignor, M.M.; Allen, S.K.; Boschung, J.; Nauels, A.; Xia, Y.; Bex, V.; Midgley, P.M. *Climate Change 2013: The Physical Science Basis: Intergovernmental Panel on Climate Change Working Group I Contribution to the Fifth Assessment Report (AR5)*; Cambridge University Press: New York, NY, USA, 2013.
4. Rao, Y.; Dai, J.; Dai, D.; He, Q. Effect of urban growth pattern on land surface temperature in China: A multi-scale landscape analysis of 338 cities. *Land Use Policy* **2021**, *103*, 105314. [CrossRef]
5. Tayyebi, A.; Shafizadeh-Moghadam, H.; Tayyebi, A.H. Analyzing long-term spatio-temporal patterns of land surface temperature in response to rapid urbanization in the mega-city of Tehran. *Land Use Policy* **2018**, *71*, 459–469. [CrossRef]
6. He, B.J.; Zhao, Z.Q.; Shen, L.D.; Wang, H.B.; Li, L.G. An approach to examining performances of cool/hot sources in mitigating/enhancing land surface temperature under different temperature backgrounds based on landsat 8 image. *Sustain. Cities Soc.* **2019**, *44*, 416–427. [CrossRef]
7. Li, J.; Feng, X.; Yin, J.; Chen, F. Change Analysis of Spring Vegetation Green-Up Date in Qinba Mountains under the Support of Spatiotemporal Data Cube. *J. Sens.* **2020**, *2020*, 6413654. [CrossRef]
8. Song, Z.; Yang, H.; Huang, X.; Yu, W.; Huang, J.; Ma, M. The spatiotemporal pattern and influencing factors of land surface temperature change in China from 2003 to 2019. *Int. J. Appl. Earth Obs. Geoinf.* **2021**, *104*, 102537. [CrossRef]
9. Guo, A.; Yang, J.; Sun, W.; Xiao, X.; Cecilia, J.X.; Jin, C.; Li, X. Impact of urban morphology and landscape characteristics on spatiotemporal heterogeneity of land surface temperature. *Sustain. Cities Soc.* **2020**, *63*, 102443. [CrossRef]
10. Peng, J.; Jia, J.; Liu, Y.; Li, H.; Wu, J. Seasonal contrast of the dominant factors for spatial distribution of land surface temperature in urban areas. *Remote Sens. Environ.* **2018**, *215*, 255–267. [CrossRef]
11. Peng, J.; Ma, J.; Liu, Q.; Liu, Y.; Hu, Y.; Li, Y.; Yue, Y. Spatial-temporal change of land surface temperature across 285 cities in China: An urban-rural contrast perspective. *Sci. Total Environ.* **2018**, *635*, 487–497. [CrossRef]
12. Yuan, G.; Tang, W.; Zuo, T.; Li, E.; Zhang, L.; Liu, Y. Impacts of afforestation on land surface temperature in different regions of China. *Agric. For. Meteorol.* **2022**, *318*, 108901. [CrossRef]
13. Zhou, S.; Liu, D.; Zhu, M.; Tang, W.; Chi, Q.; Ye, S.; Xu, S.; Cui, Y. Temporal and Spatial Variation of Land Surface Temperature and Its Driving Factors in Zhengzhou City in China from 2005 to 2020. *Remote Sens.* **2022**, *14*, 4281. [CrossRef]
14. Zhao, W.; Duan, S.-B.; Li, A.; Yin, G. A practical method for reducing terrain effect on land surface temperature using random forest regression. *Remote Sens. Environ.* **2019**, *221*, 635–649. [CrossRef]
15. Urbanski, J.A.; Wochna, A.; Bubak, I.; Grzybowski, W.; Lukawska-Matuszewska, K.; Łącka, M.; Śliwińska, S.; Wojtasiewicz, B.; Zajączkowski, M. Application of Landsat 8 imagery to regional-scale assessment of lake water quality. *Int. J. Appl. Earth Obs. Geoinf.* **2016**, *51*, 28–36.
16. He, J.; Zhao, W.; Li, A.; Wen, F.; Yu, D. The impact of the terrain effect on land surface temperature variation based on Landsat-8 observations in mountainous areas. *Int. J. Remote Sens.* **2018**, *40*, 1808–1827. [CrossRef]
17. Jamali, A.A.; Kalkhajeh, R.G.; Randhir, T.O.; He, S. Modeling relationship between land surface temperature anomaly and environmental factors using GEE and Giovanni. *J. Environ. Manag.* **2022**, *302*, 113970. [CrossRef] [PubMed]
18. Du, J.; Xiang, X.; Zhao, B.; Zhou, H. Impact of urban expansion on land surface temperature in Fuzhou, China using Landsat imagery. *Sustain. Cities Soc.* **2020**, *61*, 102346. [CrossRef]
19. Shafrina, W.M.J.W.; Nizam, A.M.K.; Marliza, M.K.A.; Asif, R.; Syarina, M.S.; Azizah, A.; Maizah, S.S.N.; Tarmizi, M.A.A.; Ayuni, J.S.N.K.; Waseem, R.K. The Influence of Deforestation on Land Surface Temperature—A Case Study of Perak and Kedah, Malaysia. *Forests* **2020**, *11*, 670.
20. Masoudi, M.; Tan, P.Y. Multi-year comparison of the effects of spatial pattern of urban green spaces on urban land surface temperature. *Landscape Urban Plan.* **2019**, *184*, 44–58. [CrossRef]
21. Peng, W.; Yuan, X.; Gao, W.; Wang, R.; Chen, W. Assessment of urban cooling effect based on downscaled land surface temperature: A case study for Fukuoka, Japan. *Urban Clim.* **2021**, *36*, 100790. [CrossRef]
22. Jung, M.C.; Dyson, K.; Alberti, M. Urban Landscape Heterogeneity Influences the Relationship between Tree Canopy and Land Surface Temperature. *Urban For. Urban Green.* **2021**, *57*, 126930. [CrossRef]
23. Peng, X.; Wu, W.; Zheng, Y.; Sun, J.; Hu, T.; Wang, P. Correlation analysis of land surface temperature and topographic elements in Hangzhou, China. *Sci. Rep.* **2020**, *10*, 10451. [CrossRef]
24. Pegau, W.S.; Paulson, C.A. The albedo of Arctic leads in summer. *Ann. Glaciol.* **2017**, *33*, 221–224. [CrossRef]
25. Lai, J.; Zhan, W.; Huang, F.; Quan, J.; Hu, L.; Gao, L.; Ju, W. Does quality control matter? Surface urban heat island intensity variations estimated by satellite-derived land surface temperature products. *ISPRS J. Photogramm. Remote Sens.* **2018**, *139*, 212–227. [CrossRef]
26. Mukherjee, F.; Singh, D. Assessing Land Use–Land Cover Change and Its Impact on Land Surface Temperature Using LANDSAT Data: A Comparison of Two Urban Areas in India. *Earth Syst. Environ.* **2020**, *4*, 385–407. [CrossRef]

27. Wu, W.; Li, L.; Li, C. Seasonal variation in the effects of urban environmental factors on land surface temperature in a winter city. *J. Clean. Prod.* **2021**, *299*, 126897. [CrossRef]
28. Chen, C.; Li, D.; Li, Y.; Piao, S.; Wang, X.; Huang, M.; Gentine, P.; Nemani, R.R.; Myneni, R.B. Biophysical impacts of Earth greening largely controlled by aerodynamic resistance. *Sci. Adv.* **2020**, *6*, eabb1981. [CrossRef] [PubMed]
29. Lemoine-Rodriguez, R.; Inostroza, L.; Zepp, H. Does urban climate follow urban form? Analysing intraurban LST trajectories versus urban form trends in 3 cities with different background climates. *Sci. Total Environ.* **2022**, *830*, 154570. [CrossRef] [PubMed]
30. Xiao, J. Satellite evidence for significant biophysical consequences of the "Grain for Green" Program on the Loess Plateau in China. *J. Geophys. Res. Biogeosci.* **2014**, *119*, 2261–2275. [CrossRef]
31. Tan, J.; Yu, D.; Li, Q.; Tan, X.; Zhou, W. Spatial relationship between land-use/land-cover change and land surface temperature in the Dongting Lake area, China. *Sci. Rep.* **2020**, *10*, 9245. [CrossRef] [PubMed]
32. Wang, L.; Chen, S.; Zhu, W.; Ren, H.; Zhang, L.; Zhu, L. Spatiotemporal variations of extreme precipitation and its potential driving factors in China's North-South Transition Zone during 1960–2017. *Atmos. Res.* **2021**, *252*, 105429. [CrossRef]
33. Li, S.; Lu, J.; Yan, J.; Liu, X.; Kong, F.; Wang, J. Spatiotemporal variability of temperature in northern and southern Qinling Mountains and its influence on climatic boundary. *Acta. Geogr. Sin.* **2018**, *73*, 13–24.
34. Jia, W.; Zhao, S. Trends and drivers of land surface temperature along the urban-rural gradients in the largest urban agglomeration of China. *Sci. Total Environ.* **2020**, *711*, 134579. [CrossRef]
35. Zhang, X.; Zhang, B.; Yao, Y.; Liu, J.; Wang, J.; Yu, F.; Li, J. Variation model of north-south plant species diversity in the Qinling-Daba Mountains in China. *Glob. Ecol. Conserv.* **2022**, *38*, e02190. [CrossRef]
36. Zhang, B. Ten major scientific issues concerning the study of China's north- south transitional zone. *Prog. Geogr.* **2019**, *38*, 305–311.
37. Zhang, X.; Zhou, J.; Liang, S.; Wang, D. A practical reanalysis data and thermal infrared remote sensing data merging (RTM) method for reconstruction of a 1-km all-weather land surface temperature. *Remote Sens. Environ.* **2021**, *260*, 112437. [CrossRef]
38. Wei, B.; Bao, Y.; Yu, S.; Yin, S.; Zhang, Y. Analysis of land surface temperature variation based on MODIS data a case study of the agricultural pastural ecotone of northern China. *Int. J. Appl. Earth Obs. Geoinf.* **2021**, *100*, 102342. [CrossRef]
39. Wang, Y.-R.; Hessen, D.O.; Samset, B.H.; Stordal, F. Evaluating global and regional land warming trends in the past decades with both MODIS and ERA5-Land land surface temperature data. *Remote Sens. Environ.* **2022**, *280*, 113181. [CrossRef]
40. Peng, S.; Gang, C.; Cao, Y.; Chen, Y. Assessment of climate change trends over the Loess Plateau in China from 1901 to 2100. *Int. J. Climatol.* **2018**, *38*, 2250–2264. [CrossRef]
41. He, J.; Yang, K.; Tang, W.; Lu, H.; Qin, J.; Chen, Y.; Li, X. The first high-resolution meteorological forcing dataset for land process studies over China. *Sci. Data* **2020**, *7*, 25. [CrossRef]
42. Chen, J.; Chen, J.; Liao, A.; Cao, X.; Chen, L.; Chen, X.; He, C.; Han, G.; Peng, S.; Lu, M.; et al. Global land cover mapping at 30m resolution: A POK-based operational approach. *ISPRS J. Photogramm. Remote Sens.* **2015**, *103*, 7–27. [CrossRef]
43. Zheng, K.; Tan, L.; Sun, Y.; Wu, Y.; Duan, Z.; Xu, Y.; Gao, C. Impacts of climate change and anthropogenic activities on vegetation change: Evidence from typical areas in China. *Ecol. Indic.* **2021**, *126*, 107648. [CrossRef]
44. Zhao, B.; Mao, K.; Cai, Y.; Meng, X. Study of the temporal and spatial evolution law of land surface temperature in China. *Remote Sens. Land Resour.* **2020**, *32*, 233–240.
45. Wang, J.F.; Li, X.H.; Christakos, G.; Liao, Y.L.; Zhang, T.; Gu, X.; Zheng, X.Y. Geographical Detectors-Based Health Risk Assessment and its Application in the Neural Tube Defects Study of the Heshun Region, China. *Int. J. Geogr. Inf. Sci.* **2010**, *24*, 107–127. [CrossRef]
46. He, W.; Meng, H.; Han, J.; Zhou, G.; Zheng, H.; Zhang, S. Spatiotemporal PM2.5 estimations in China from 2015 to 2020 using an improved gradient boosting decision tree. *Chemosphere* **2022**, *296*, 134003. [CrossRef]
47. Chen, W.; Meng, H.; Song, H.; Zheng, H. Progress in Dust Modelling, Global Dust Budgets, and Soil Organic Carbon Dynamics. *Land* **2022**, *11*, 176. [CrossRef]
48. Abera, T.A.; Heiskanen, J.; Pellikka, P.; Rautiainen, M.; Maeda, E.E. Clarifying the role of radiative mechanisms in the spatio-temporal changes of land surface temperature across the Horn of Africa. *Remote Sens. Environ.* **2019**, *221*, 210–224. [CrossRef]
49. Zhang, T.; Barry, R.G.; Gilichinsky, D.; Bykhovets, S.; Sorokovikov, V.; Ye, J. An amplified signal of climatic change in soil temperatures during the last century at Irkutsk, Russia. *Clim. Chang.* **2001**, *49*, 41–76.
50. Wang, Z.; Sun, D.; Hu, C.; Wang, Y.; Zhang, J. Seasonal Contrast and Interactive Effects of Potential Drivers on Land Surface Temperature in the Sichuan Basin, China. *Remote Sens.* **2022**, *14*, 1292.
51. Tian, H.; Liu, L.; Zhang, Z.; Chen, H.; Zhang, X.; Wang, T.; Kang, Z. Spatiotemporal diversity of land surface temperature in China from 2001 to 2020. *Acta Geogr. Sin.* **2022**, *77*, 1713–1729.
52. Cao, J.; Zhou, W.; Zheng, Z.; Ren, T.; Wang, W. Within-city spatial and temporal heterogeneity of air temperature and its relationship with land surface temperature. *Landsc. Urban Plan.* **2021**, *206*, 103979. [CrossRef]
53. Dong, J.; Liu, P.; Song, H.; Yang, D.; Yang, J.; Song, G.; Miao, C.; Zhang, J.; Zhang, L. Effects of anthropogenic precursor emissions and meteorological conditions on $PM_{2.5}$ concentrations over the "2+26" cities of northern China. *Environ. Pollut.* **2022**, *315*, 120392. [CrossRef] [PubMed]
54. Venkatesh, K.; John, R.; Chen, J.; Xiao, J.; Amirkhiz, R.G.; Giannico, V.; Kussainova, M. Optimal ranges of social-environmental drivers and their impacts on vegetation dynamics in Kazakhstan. *Sci. Total Environ.* **2022**, *847*, 157562. [CrossRef] [PubMed]
55. Zhao, W.; Duan, S.B. Reconstruction of daytime land surface temperatures under cloud-covered conditions using integrated MODIS/Terra land products and MSG geostationary satellite data. *Remote Sens. Environ.* **2020**, *247*, 111931. [CrossRef]

56. Zeng, C.; Long, D.; Shen, H.; Wu, P.; Cui, Y.; Hong, Y. A two-step framework for reconstructing remotely sensed land surface temperatures contaminated by cloud. *ISPRS J. Photogramm. Remote Sens.* **2018**, *141*, 30–45. [CrossRef]
57. Hidalgo-García, D.; Arco-Díaz, J. Modeling the Surface Urban Heat Island (SUHI) to study of its relationship with variations in the thermal field and with the indices of land use in the metropolitan area of Granada (Spain). *Sustain. Cities Soc.* **2022**, *87*, 104166. [CrossRef]
58. Yang, M.; Zhao, W.; Zhan, Q.; Xiong, D. Spatiotemporal Patterns of Land Surface Temperature Change in the Tibetan Plateau Based on MODIS/Terra Daily Product From 2000 to 2018. *IEEE J. Sel. Top. Appl. Earth Obs. Remote Sens.* **2021**, *14*, 6501–6514. [CrossRef]
59. Zhou, D.; Xiao, J.; Bonafoni, S.; Berger, C.; Deilami, K.; Zhou, Y.; Frolking, S.; Yao, R.; Qiao, Z.; Sobrino, J.A. Satellite remote sensing of surface urban heat islands: Progress, challenges, and perspectives. *Remote Sens.* **2018**, *11*, 48. [CrossRef]
60. Mohamed, A.A.; Odindi, J.; Mutanga, O. Land surface temperature and emissivity estimation for Urban Heat Island assessment using medium- and low-resolution space-borne sensors: A review. *Geocarto Int.* **2016**, *32*, 455–470. [CrossRef]